Received: 22 April 2024 | Revised: 15 August 2024 | Accepted: 16 August 2024

DOI: 10.1002/mrm.30282

Magnetic Resonance in Medicine

TECHNICAL NOTE

Spiral 3DREAM sequence for fast whole-brain B1 mapping

Svenja Niesen[1] | **Marten Veldmann**[1] | **Philipp Ehses**[1] | **Tony Stöcker**[1,2]

[1]MR Physics, German Center for Neurodegenerative Diseases (DZNE), Bonn, Germany

[2]Department of Physics & Astronomy, University of Bonn, Bonn, Germany

Correspondence
Tony Stöcker, German Center for Neurodegenerative Diseases (DZNE), MR Physics, Venusberg-Campus 1, Gebäude 99, 53127 Bonn, Germany.
Email: tony.stoecker@dzne.de

Abstract

Purpose: This work demonstrates a new variant of the 3DREAM sequence for whole-brain B_1^+ mapping employing a three-dimensional (3D) stack-of-spirals readout. The spiral readout reduces the echo train length after the STEAM preparation in order to overcome the significant blurring in STE* images due to the decreasing STE* signal with each excitation pulse.

Methods: The 3DREAM sequence rapidly acquires two contrasts to calculate whole-brain flip angle maps. In the proposed spiral 3DREAM sequence, the Cartesian readout scheme is replaced by an accelerated 3D stack-of-spirals readout with a CAIPIRINHA sampling scheme. Phantom experiments were conducted to compare flip angle maps of the spiral 3DREAM sequence to a Cartesian 3DREAM sequence, an actual flip-angle-imaging (AFI) sequence, the dual-angle method, and the Bloch–Siegert shift method. Afterwards, the results were validated in vivo acquiring flip angle maps from five subjects.

Results: Flip angle maps of the spiral 3DREAM sequences showed high agreement with the reference methods both in phantom and in vivo experiments. Blurring in STE* images and flip angle maps was reduced compared to the Cartesian 3DREAM sequence.

Conclusion: The spiral 3DREAM sequence utilizes a fast readout minimizing the echo train length of the imaging train. This reduces blurring in STE* images as well as the total acquisition time and increases the effective resolution of B_1^+ maps.

KEYWORDS

3DREAM, B_1^+ mapping, sequence development, spiral imaging

1 | INTRODUCTION

The measurement of the applied radiofrequency (RF) field (B_1^+) is important for different MRI applications, including accurate scaling of RF power to achieve the desired flip angle[1] and, particularly, quantitative MR imaging.[2] B_1^+ maps are also used on parallel transmit systems for static RF shimming or the calculation of dynamic pTx pulses.[3]

The different approaches for the measurement of RF fields can be divided into magnitude- and phase-based methods. Magnitude-based methods include the (saturated) dual-angle B_1^+ mapping method based on a

Svenja Niesen and Marten Veldmann contributed equally to this work.

GRE acquisition,[4,5] the actual flip-angle-imaging (AFI) method,[6] and the RF-prepared three-dimensional (3D) FLASH acquisition.[7] The phase-sensitive method developed by Morell[8] and B_1^+ mapping based on the Bloch–Siegert shift (BSS)[9] are examples for phase-based methods. Several approaches for flip angle mapping are based on a stimulated echo (STE) signal.[10–14] One of these approaches is the dual refocusing echo acquisition mode (DREAM) sequence,[14] which consists of a STEAM preparation, followed by a low-angle imaging pulse train acquiring two signals—the free induction decay (FID) and the virtual stimulated echo (STE*). Separating B_1^+ and spatial encoding weakens the specific absorption rate (SAR) burden and the quasi-simultaneously measurement of the two signals accelerates the scan and allows for volumetric B_1^+ mapping.[14,15] The volumetric DREAM sequence[15] uses slice-selective pulses both for the STEAM preparation and for the imaging train and an interleaved slice acquisition order. Recently, DREAM has been extended to the 3DREAM sequence with a 3D readout[16] allowing for rapid whole-brain B_1^+ mapping. In the 3DREAM sequence, a single STEAM preparation with nonselective block pulses is applied before the 3D Cartesian imaging train. As a result, the STE* signal decreases as it is "consumed" with each excitation, whereas the FID signal evolves toward a steady state.[16] The STE* decay is mainly determined by the excitation flip angle, the number of total excitations (echo train length—ETL), T_1 and TR[16] and can result in strong blurring leading to artifacts in resulting flip angle maps. One solution to compensate for the different evolution of FID and STE* signals, is to apply a filter on the FID images to align blurring levels,[16] however, decreasing the effective resolution.

The approach used in this work is based on the 3DREAM sequence and differs in terms of k-space acquisition in the imaging train. Instead of a Cartesian two phase encoding order, a non-Cartesian 3D stack-of-spirals readout is used to acquire the STE* and FID signals. Non-Cartesian k-space acquisition with spiral k-space trajectories benefits from short scan duration compared to conventional spin-warp sequences.[17] This advantage is used for the 3DREAM sequence to decrease the ETL and counteract the fast decay of the STE* signal[16] for reduced blurring and a higher effective resolution of B_1^+ maps.

2 | METHODS

2.1 | Implementation of spiral 3DREAM

Figure 1 shows the spiral 3DREAM sequence. The STEAM preparation is the same as in the original Cartesian 3DREAM[16] using two nonselective block pulses. Fat saturation before the first STEAM preparation pulse (not shown) and two slab-selective binomial pulses for water-specific excitation[18] are used to reduce chemical shift artifacts.

The STE* signal is dephased by the first gradient G_M on the slice axis. The gradient G_{-M} has the same absolute gradient moment with opposite sign and thus rephases the STE* signal, while dephasing the FID signal:

$$\int G_M \, dt = -\int G_{-M} \, dt. \quad (1)$$

The FID signal is rephased with the second gradient G_M. G_M and G_{-M} are further referred to as "signal separation gradients." In contrast to the original 3DREAM, these gradients were applied along the slice direction to reduce eddy current effects on the spiral trajectory.

The STE* and FID signals were acquired with an accelerated 3D stack-of-spirals readout. Since the STE* and FID had the same effective TE, the flip angle quantification was T_2 compensated.[15] A dual-echo GRE reference scan was acquired before the spiral 3DREAM to calculate coil sensitivity and B_0 field maps. The spiral 3DREAM was implemented in Pulseq.[19,20]

2.2 | Reconstruction

Reconstruction was done with an iterative SENSE reconstruction[21] using the PowerGrid toolbox.[22] The reconstruction included a time-segmented B_0 correction[23] with the B_0 map calculated from the dual-echo GRE reference scan. Coil sensitivity maps were calculated from the first echo of the reference scan with the ESPIRiT algorithm.[24] Image reconstruction was implemented as part of an open-source imaging workflow.[25]

To equalize blurring due to different signal evolution of STE* and FID, the FID images were filtered after reconstruction using a global filter as proposed in Reference 16.

2.3 | Phantom experiments

All measurements were performed on a MAGNETOM 7T Plus scanner (Siemens Healthineers AG, Germany) with a 32-channel receive, single-channel transmit coil (Nova Medical) on a homogeneous phantom[26] (Table S1). Flip angle maps were acquired with the spiral and Cartesian 3DREAM at an isotropic resolution of 5 mm (field of view: $200 \times 200 \times 200\,mm^3$). The dual-angle method (DAM),[4] the BSS method[9] and an AFI sequence[6] were used as reference methods.

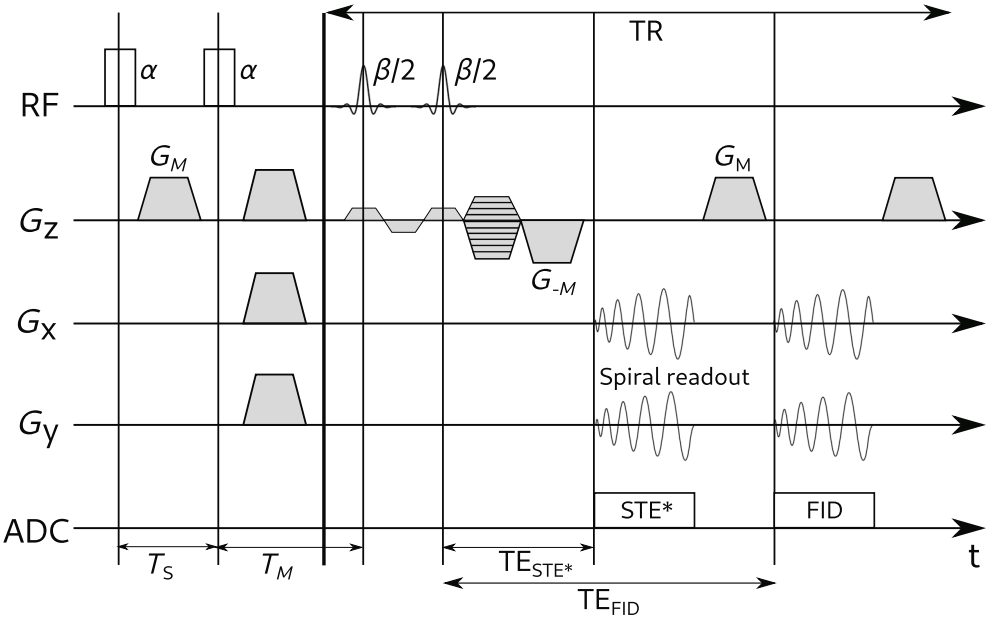

FIGURE 1 The spiral 3DREAM sequence starts with a STEAM preparation sequence with nonselective block pulses (flip angle α) followed by a spiral imaging train. Here, T_S is the STEAM preparation pulse interval and T_M is the mixing time. Fat saturation before the STEAM preparation (not shown) and binomial (1-1) pulses (flip angle β) at the beginning of the spiral imaging train are used to suppress fat signal. The gradients G_M and G_{-M} have equal absolute gradient moments with opposite sign leading to a separation of the two signals in k-space. In the sequence utilized at the scanner, the phase encoding gradient, the second slab selection rephaser and the gradient G_{-M} were merged into one gradient.

The spiral 3DREAM data were acquired in transversal orientation with flip angles $\alpha = 50°$ and $\beta = 5°$ ($TE_{STE^*} = 0.72$ ms, $TE_{FID} = 4.28$ ms). The spiral readout consisted of one interleaf per partition with an in-plane acceleration of $R_{int} = 5$ and without additional acceleration in phase-encoding direction ($R_{Ph} = 1$). A controlled aliasing in parallel imaging results in higher acceleration (CAIPIRINHA)-shift of $\delta = 4$ was applied[27] by using different sets of spiral interleaves in subsequent partitions (partition 1: first interleaf, partition 2: fifth interleaf, etc.). The ETL was 40 and the acquisition time (TA) excluding the reference scan was 0.33 s. The reference scan was acquired at the same field of view and resolution as the spiral scan. All sequence parameters can be found in Table S2.

The Cartesian 3DREAM data was acquired in sagittal orientation with nonselective pulses in the imaging train ($TE_{STE^*} = 1.06$ ms, $TE_{FID} = 2.26$ ms). An acceleration factor of $R = 2 \times 2$ in phase encoding directions led to an ETL of 400 and TA of 1.33 s. A CAIPIRINHA-shift of $\delta = 1$ was applied (implemented as in Reference 16). Flip angles α and β were the same as in the spiral sequence. Compared to the original 3DREAM,[16] a spoiling moment was added to the signal separation gradients in readout direction to better separate STE* and FID signals (Figure S1).

AFI flip angle maps were obtained using a flip angle of 50°, an acceleration factor of $R = 2$, $TR_1 = 20$ ms, $TR_2 = 100$ ms, TE = 0.97 ms and TA = 80 s. The BSS sequence acquired two images with ±5 kHz off-resonant Fermi pulses (peak $B_1^+ = 7.72$ µT), an imaging flip angle of 20°, TE = 6.25 ms and TR = 100 ms. For the DAM, two 3D-GRE scans with flip angles 60° and 120° were acquired. TE = 0.95 ms and TR = 4 s were chosen to allow for almost full relaxation considering $T_1 = 840$ ms of the phantom. Both scans resulted in TA = 42 min.

Flip angle maps of both 3DREAM sequences were compared with the reference methods using scatterplots, Pearson correlation coefficients and a linear fit for which the root-mean-square error (RMSE) was calculated. A centrally located sphere with a radius of ten voxels was selected as the region of interest, as signal dropouts were observed outside this sphere due to the high dynamic range of B_1^+ in the phantom.[26] All flip angle maps were registered to the magnitude image of the AFI sequence using FSL FLIRT[28] and a brain mask[29] followed by an eroding kernel, which was applied onto the maps.

To investigate the impact of acceleration on the flip angle maps obtained from the spiral 3DREAM, a nonaccelerated spiral scan was acquired (ETL: 200). The nonaccelerated scan was additionally executed with a segmented acquisition to keep the ETL per segment the same as in the accelerated scan. The segmented version consisted of five segments each with an own STEAM preparation and a waiting time of 3 s in-between segments to allow for relaxation.

The repeatability of B_1^+ mapping with the accelerated spiral 3DREAM sequence was investigated by repeating the measurement in a second scan session on a different day (test–retest). The intraclass correlation coefficient[30] for two-way mixed effects, single raters, was calculated and a Bland–Altman plot along with the reproducibility coefficient and the coefficient of variation was created to evaluate the repeatability of flip angle maps in test and retest measurements.

2.4 | In vivo experiments

In vivo data were acquired with both 3DREAM sequences and the AFI sequence from five healthy volunteers (three male, two female, age between 24 and 48) after giving informed consent. The DAM and BSS were not performed in vivo. For the DAM the acquisition time was too high, making it susceptible to motion, and for the BSS the energy of the off-resonant pulses was too low for accurate flip angle mapping due to specific absorption rate constraints.

Data were acquired at 5 and 3 mm isotropic resolution. The parameters of the scan at 5 mm resolution were the same as for the phantom experiments, but one interleaf with $R_{\text{int}} = 6$, $R_{\text{Ph}} = 1$ and $\delta = 5$ were chosen ($TE_{STE^*} = 0.72$ ms, $TE_{FID} = 3.96$ ms, ETL = 40, TA = 0.30 s). The scan at 3 mm resolution had a field of view of $216 \times 216 \times 216$ mm^3. The spiral sequence parameters were: $TE_{STE^*} = 0.88$ ms, $TE_{FID} = 6.28$ ms, ETL = 72, TA = 0.87 s. The resolution of the spiral reference scan was limited to 4.32 mm to not excessively increase scan time. The acceleration of the Cartesian 3DREAM was increased to $R = 2 \times 4$ with $\delta = 2$ to decrease the ETL ($TE_{STE^*} = 1.25$ ms, $TE_{FID} = 2.5$ ms, ETL = 648, TA = 2.39 s). All other parameters of both 3DREAM sequences were kept the same as for the 5 mm in vivo scan. The parameters of the AFI sequence were kept the same as in the phantom experiments except for TE = 1.10 ms, resulting in TA = 4 min for the scan with 3 mm resolution. To investigate the effect of blurring in the STE* image, FID images of both 3DREAM sequences were reconstructed with and without the global filter and the high-frequency error norm was calculated.[31] The global filter was applied onto synthesized k-space data as it describes the STE* decay and blurring of both 3DREAM sequences was compared with the FWHM of the reconstructed point object for 3 and 5 mm.

We observed different artifacts especially in the STE* images of the Cartesian and spiral 3DREAM depending on the moment and orientation of the signal separation gradients. Therefore, we acquired (a) the spiral 3DREAM with these gradients either in slice (G_z) or in one of the readout directions (G_x) and (b) the Cartesian 3DREAM with and without the spoiling moment added to the gradients (Figure S1). Changing the signal separation gradients required a slight adjustment of the timing parameters (spiral 3DREAM: label "5 mm (RO)" in Table S2; Cartesian 3DREAM: $TE_{STE^*} = 1.37$ ms, $TE_{FID} = 2.46$ ms).

Flip angle maps of the 3DREAM sequences and the AFI were compared as in the phantom experiments.

3 | RESULTS

Figure 2 shows flip angle maps of one coronal and transversal slice in the phantom's center. The Pearson correlation coefficients and the linear fits indicate high agreement of both 3DREAM sequences with the reference methods. The slope of the linear fits of the spiral 3DREAM was higher compared to the Cartesian 3DREAM for all comparisons, however, in the AFI comparison, the RMSE was slightly increased for the spiral 3DREAM. For both 3DREAM sequences, but enhanced for the spiral 3DREAM, the coronal image contained a region with increased blurring at the bottom of the phantom, where low flip angles were observed.

Figure S2 shows the results for the nonaccelerated, accelerated, and nonaccelerated segmented spiral scans. The accelerated scan had a similar Pearson correlation coefficient and RMSE, but higher slope in the comparison with the AFI as the nonaccelerated segmented scan. An artifact (white arrow) was observed at the bottom of the phantom in the accelerated scan. The nonaccelerated nonsegmented scan showed significantly stronger blurring compared to the accelerated and segmented scans and underestimated high flip angles when compared to the AFI. The results of the spiral 3DREAM test–retest measurements are shown in a Bland–Altman plot (Figure S3). The plot demonstrates larger differences at lower angles and an absolute mean difference close to zero. The intraclass correlation coefficient (0.993), reproducibility coefficient (3.139 °), and coefficient of variation (5.426 %) imply excellent test–retest reliability.

Figure 3 shows flip angle maps of one subject at 3 and 5 mm resolution acquired with the AFI and both 3DREAM sequences and the corresponding scatterplots. Overall, the flip angle distribution was similar for all three sequences with larger flip angles in the center of the brain and lower flip angles present in peripheral parts of the brain. 3DREAM flip angle maps at both resolutions showed some ventricular contrast, which was more pronounced in the Cartesian 3DREAM and stronger at 3 mm resolution compared to 5 mm resolution. The high agreement of both 3DREAM sequences with the AFI was reflected in high correlation coefficients and low RMSE (Table 1). Both 3DREAM sequences performed similarly,

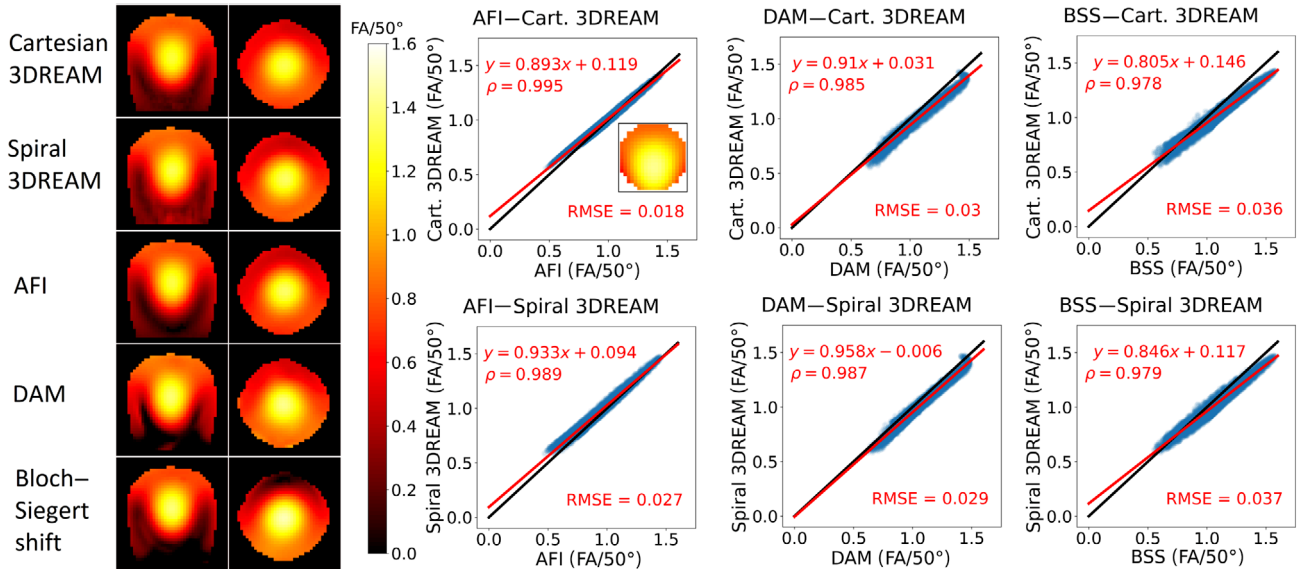

FIGURE 2 Left: Flip angle maps of the 3DREAM sequences, the actual flip-angle-imaging (AFI), the dual-angle method (DAM), and the Bloch–Siegert shift (BSS) with an isotropic resolution of 5 mm for one coronal and one transversal slice. Right: Scatterplots comparing flip angle maps of the 3DREAM sequences to the three reference methods. The linear fit is shown as a red line alongside with the fit parameters and correlation coefficients ρ. The black line is the identity. A sphere, centered in the middle of the phantom and with a radius of ten voxels is selected for the comparison. The selected region for the comparison is shown in the inset of the first scatterplot.

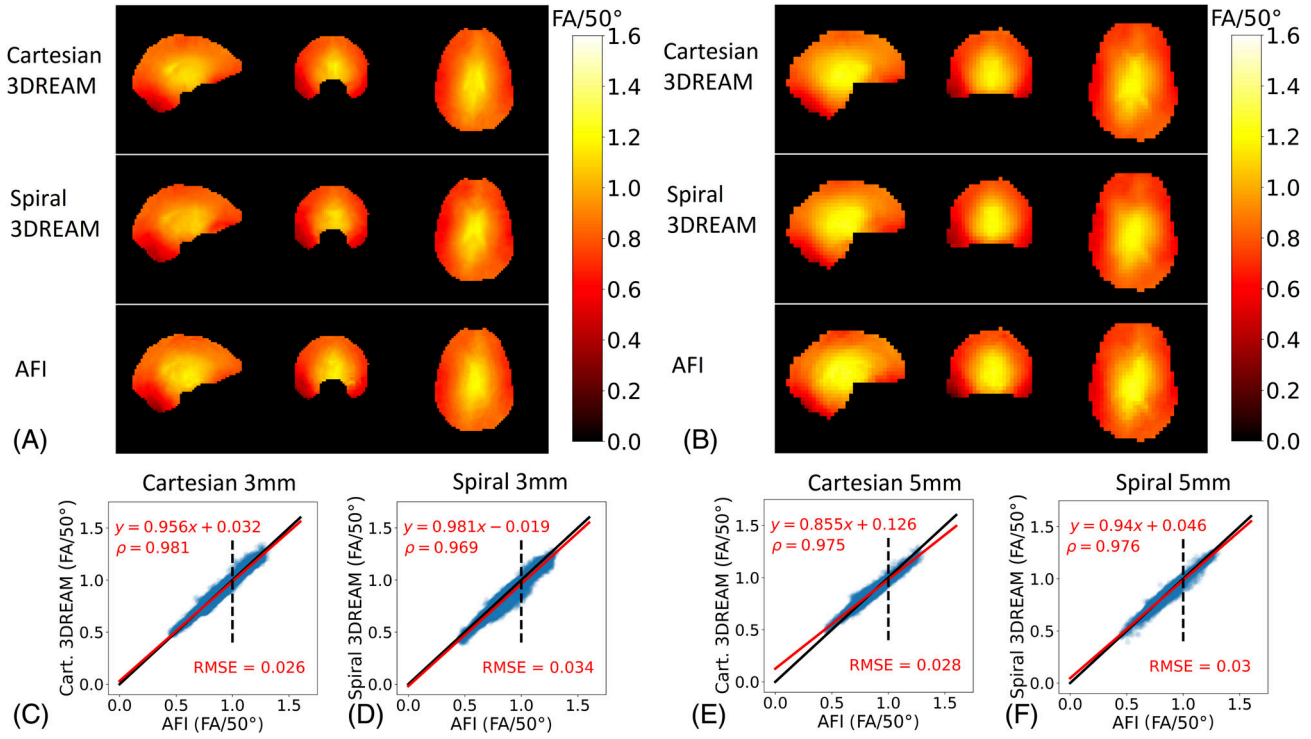

FIGURE 3 Top row: Normalized flip angle maps of subject 5 at (A) 3 mm and (B) 5 mm resolution from the Cartesian 3DREAM at the top, the spiral 3DREAM in the middle and the AFI in the bottom row. One central slice for each view (sagittal, coronal and transversal) is presented. Bottom row: Linear fits for the comparison of the masked flip angle maps with normalized axes for 3 mm (C,D) and 5 mm (E,F) resolution. The linear fit is shown as a red line alongside with the fit parameters and correlation coefficients ρ. The black line is the identity. In addition, the dashed line marks the flip angle 50° and thus the beginning of the underestimation at higher flip angles.

TABLE 1 Subject information including the subject number (#), age, gender (f: female, m: male) and the results of the linear fit for the comparison of Cartesian 3DREAM and AFI (C-A) and spiral 3DREAM and AFI (S-A) are shown for all five subjects.

			Slope		Intercept		ρ		RMSE	
#	Age	Gender	C-A	S-A	C-A	S-A	C-A	S-A	C-A	S-A
1	24	f	0.91	0.96	0.09	0.03	0.98	0.97	0.03	0.04
			0.87	0.91	0.10	0.07	0.98	0.98	0.03	0.03
2	28	m	0.86	0.91	0.09	0.03	0.97	0.96	0.03	0.03
			0.84	0.84	0.12	0.12	0.96	0.96	0.03	0.04
3	26	m	0.86	0.87	0.10	0.08	0.97	0.97	0.03	0.03
			0.81	0.84	0.17	0.16	0.97	0.97	0.03	0.03
4	48	f	0.85	0.86	0.10	0.07	0.98	0.97	0.03	0.03
			0.83	0.84	0.14	0.12	0.97	0.97	0.03	0.03
5	41	m	0.96	0.98	0.03	-0.02	0.98	0.97	0.03	0.03
			0.86	0.94	0.13	0.05	0.98	0.98	0.03	0.03

Notes: Listed are the slope and the intercept of the fit, the Pearson correlation coefficient ρ and the RMSE for 3 mm resolution in the first row of each subject and 5 mm resolution in the second row accordingly.

however the spiral 3DREAM had a slope closer to one and lower intercepts. A slight systematic underestimation at high flip angles (>50°, dashed line) was most visible for the Cartesian 3DREAM at 5 mm resolution.

Figure 4I shows in vivo STE* and FID images of both 3DREAM sequences, acquired at an isotropic resolution of 3 mm. The contrast of both STE* and FID was different between the two 3DREAM sequences due to the difference in TE. In the spiral data the white to gray matter contrast was higher in FID images compared to the Cartesian sequence. Blurring in spiral STE* images was less pronounced than in Cartesian STE* images. This becomes apparent comparing the filtered FID images, where the blurring levels were aligned to the STE* images and comparing the high-frequency error norm: (Cartesian: 0.805, spiral: 0.386). The global filter did not alter the spiral FID signal as strong as the Cartesian FID. At 5 mm resolution the blurring was decreased (Figure S4, high-frequency error norm: Cartesian: 0.639, spiral: 0.100). These observations meet the lower FWHM of a global filtered point object for the spiral 3DREAM compared to the Cartesian 3DREAM (Figure S5C).

Figure 4II presents results with and without modified signal separation gradients at 5 mm resolution. Ring-shaped artifacts (red arrows) in readout direction (yellow arrows) appeared in the STE* images without modification of the signal separation gradients. For the Cartesian 3DREAM, the artifact was located at the top of the head (a) and for the spiral 3DREAM, it was located near the ear region (b). These artifacts were not visible in the FID images, but translated to the flip angle maps.

4 | DISCUSSION

The results demonstrate accurate B_1^+ quantification with the spiral 3DREAM sequence with high statistical agreement to reference sequences, here the AFI, DAM, and BSS. In phantom experiments, the reduction of the ETL in the spiral 3DREAM compared to the Cartesian 3DREAM, combined with one spiral interleaf in-plane, led to an increased slope of the fit, indicating less underestimated flip angles due to less filtering of STE* near the k-space center.[15] As demonstrated in Figure S5B, the trajectory led to reduced blurring. The small RMSE differences of the 3DREAM sequences originate mostly from voxels with lower flip angles. As demonstrated in the Bland–Altman plot, the computation precision decreases at low STE* signal. The registration partly smoothes these regions leading to small RMSE differences of the 3DREAM sequences.

The results from the phantom experiment with the accelerated, nonaccelerated and nonaccelerated segmented version of the spiral sequence justify the choice of the acceleration factor. Results from the accelerated scan were close to results of the nonaccelerated segmented version, except for an artifact in a low-SNR region, but with a slope closer to one, which might be attributed to motion artifacts in the segmented scan.[16] Additionally, TA of the segmented scan increases due to waiting time between segments.[16] The long ETL combined with five in-plane interleaves of the nonaccelerated nonsegmented scan resulted in significantly increased blurring and underestimated high flip angles as less signal was present in k-space. The test–retest demonstrated high repeatability and a lack of systematic errors.

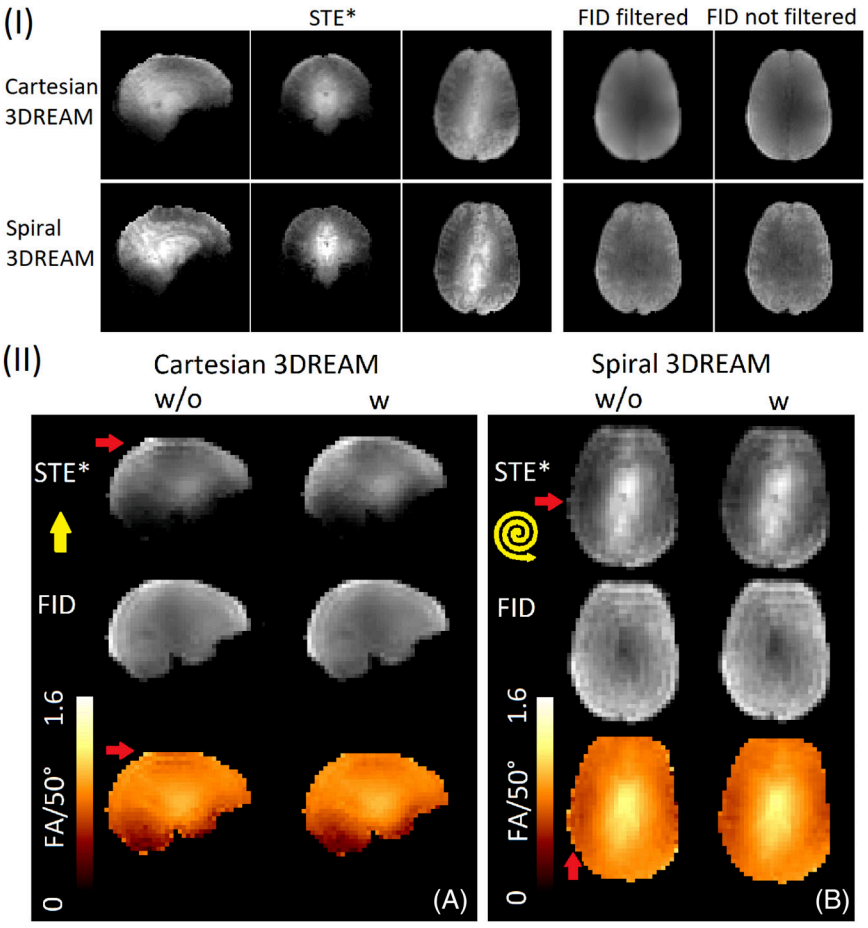

FIGURE 4 (I) One sagittal, coronal and transversal slice of the STE* at 3 mm resolution is shown for both Cartesian (top) and spiral (bottom) 3DREAM sequences. Additionally, the transversal slice of the free induction decay (FID) is displayed on the right, with and without the FID filter applied. (II) (A) Sagittal STE* and FID images at 5 mm resolution as well as normalized flip angle maps of the Cartesian 3DREAM sequence without (w/o) and with (w) modified signal separation gradients. The red arrows point to the ring-shaped artifacts in the STE* images and in the flip angle maps. The yellow arrow indicates the readout direction. (B) The same results are shown for the spiral sequence, but a transversal slice is displayed as the readout direction differs from the Cartesian sequence. All images were obtained from subject 5.

The flip angle maps of the 3DREAM and AFI were in high agreement in vivo as well. In References 15 and 16, the observed ventricular contrast is attributed partly to tissue properties, but also to an increased T_1 and T_2 decay of the STE*. As can be seen in Figure S5C, the spiral 3DREAM leads to less STE* decay compared to the Cartesian 3DREAM, explaining the reduced ventricular contrast, especially at 3 mm resolution. Due to the lower ETL, the 5 mm flip angle maps suffered less from the STE* decay, but both 3DREAM sequences performed well also at 3 mm resolution. Due to less STE* signal filtering near the k-space center, the slope of the spiral 3DREAM fit is increased, indicating a lower flip angle underestimation.[15] As in the phantom experiments, the spiral 3DREAM shows a slightly higher RMSE than the Cartesian 3DREAM after registration. Despite using six interleaves, the higher TE of the spiral 3DREAM increases the RMSE in regions with lower T_2^*, but only to a small extent. Using more interleaves would decrease TE, but increases ETL leading to more STE* blurring. Higher acceleration decreases blurring, but is limited by coil sensitivities and decreased SNR.

As demonstrated in Reference 16, applying the correct global filter on the FID eliminates erroneous flip angles at the edge of the brain. The flip angle maps demonstrate equalized blurring for both contrasts using the global filter for the spiral 3DREAM as presented for the Cartesian 3DREAM in Reference 16. As the ETL was significantly shorter in spiral acquisitions, a much weaker filter was needed, which increased the effective resolution of the flip angle maps. Both the TR and the ETL are essential parameters determining the blurring in the images, however, as can be seen in Figure S5C, the impact of the shorter ETL of the spiral 3DREAM leads to a stronger blurring reduction than the reduced TR of the Cartesian 3DREAM.

The observed ring-shaped artifacts in STE* images and flip angle maps, are attributed to folding of FID and STE* signals in k-space. Particularly, the dominant FID signal folds into the STE* signal. Applying the signal separation gradients of the spiral 3DREAM in slice direction instead of in readout direction led to a better separation of the FID and STE* k-spaces. This also reduced eddy current effects of the spoilers on the spiral readout, as cross-responses from other gradient axes are typically small.[32] The improved separation of k-spaces with an additional spoiling moment in the Cartesian 3DREAM reduced artifacts in a similar way.

The RF-prepared 3D FLASH method[7] has a wider dynamic range and includes correction for ventricular contrast. Similar to 3DREAM it acquires whole brain flip angle maps in seconds, however, it requires two shots, which increases motion sensitivity. In contrast, 3DREAM acquires both contrasts in one shot.

5 | CONCLUSIONS

An extension of the 3DREAM sequence with a stack-of-spirals readout was presented. The spiral 3DREAM produced comparable B_1^+ mapping results to the existing Cartesian 3DREAM and to other established methods such as AFI. Comparing the 3DREAM sequences, the Cartesian 3DREAM with its shorter TE is more robust against low T_2^* regions than the spiral 3DREAM. However, the reduced ETL of the spiral 3DREAM leads to less filtering of high k-space frequencies, reducing the blurring in all encoding directions and the ventricular contrast. This allows for a higher effective resolution and also reduces filtering near the k-space center, reducing underestimation of high flip angles.

ACKNOWLEDGMENTS

The authors thank the ISMRM Reproducible Research Study Group for conducting a code review of the code (MRM release v2, DOI: 10.5281/zenodo.8422024) supplied in the Data Availability Statement. The scope of the code review covered only the code's ease of download, quality of documentation, and ability to run, but did not consider scientific accuracy or code efficiency. Open Access funding enabled and organized by Projekt DEAL.

CONFLICT OF INTEREST STATEMENT

The authors declare no potential conflict of interests.

DATA AVAILIBILITY STATEMENT

The sequence designed with Pulseq can be found in the following openly available Github repository: https://github.com/mrphysics-bonn/spiral3dream/tree/mrm_v3 (DOI: 10.5281/zenodo.13304406).

ORCID

Svenja Niesen https://orcid.org/0009-0001-3094-1333
Marten Veldmann https://orcid.org/0000-0003-2444-9649
Philipp Ehses https://orcid.org/0000-0002-5839-6525
Tony Stöcker https://orcid.org/0000-0002-8946-9141

REFERENCES

1. Slayman BE, King KF, Licato PE. Nutation angle measurement during MRI prescan. US Patent 5,416,412. May 16 1995.
2. Shah B, Anderson SW, Scalera J, Jara H, Soto JA. Quantitative MR imaging: physical principles and sequence design in abdominal imaging. *Radiographics*. 2011;31:867-880. doi:10.1148/rg.313105155
3. Katscher U, Börnert P. Parallel RF transmission in MRI. *NMR Biomed*. 2006;19:393-400. doi:10.1002/nbm.1049
4. Stollberger R, Wach P, McKinnon G, Justich E, Ebner F. RF-field mapping in vivo. *Proceedings of the 7th Annual Scientific Meeting and Exhibition*. Elsevier; 1988:106.
5. Cunningham CH, Pauly JM, Nayak KS. Saturated double-angle method for rapid B1+ mapping. *Magn Reson Med*. 2006;55:1326-1333. doi:10.1002/mrm.20896
6. Yarnykh VL. Actual flip-angle imaging in the pulsed steady state: a method for rapid three-dimensional mapping of the transmitted radiofrequency field. *Magn Reson Med*. 2007;57:192-200. doi:10.1002/mrm.21120
7. Zhu D, Schär M, Qin Q. Ultrafast B1 mapping with RF-prepared 3D FLASH acquisition: correcting the bias due to T1-induced k-space filtering effect. *Magn Reson Med*. 2022;88:757-769. doi:10.1002/mrm.29247
8. Morrell GR. A phase-sensitive method of flip angle mapping. *Magn Reson Med*. 2008;60:889-894. doi:10.1002/mrm.21729
9. Sacolick LI, Wiesinger F, Hancu I, Vogel MW. B1 mapping by Bloch-Siegert shift. *Magn Reson Med*. 2010;63:1315-1322. doi:10.1002/mrm.22357
10. Akoka S, Franconi F, Seguin F, Le Pape A. Radiofrequency map of an NMR coil by imaging. *Magn Reson Imaging*. 1993;11:437-441. doi:10.1016/0730-725X(93)90078-R
11. Jiru F, Klose U. Fast 3D radiofrequency field mapping using echo-planar imaging. *Magn Reson Med*. 2006;56:1375-1379. doi:10.1002/mrm.21083
12. Helms G, Finsterbusch J, Weiskopf N, Dechent P. Rapid radiofrequency field mapping in vivo using single-shot STEAM MRI. *Magn Reson Med*. 2008;60:739-743. doi:10.1002/mrm.21676
13. Nehrke K, Boernert P. Fast B1 mapping using a STEAM-based Bloch-Siegert preparation pulse. *Proceedings of the 19th Annual Meeting of ISMRM*. ISMRM; 2011:4411.
14. Nehrke K, Börnert P. DREAM-a novel approach for robust, ultrafast, multislice B1 mapping. *Magn Reson Med*. 2012;68:1517-1526. doi:10.1002/mrm.24158
15. Nehrke K, Versluis MJ, Webb A, Börnert P. Volumetric B1+ mapping of the brain at 7T using DREAM. *Magn Reson Med*. 2014;71:246-256. doi:10.1002/mrm.24667
16. Ehses P, Brenner D, Stirnberg R, Pracht ED, Stöcker T. Whole-brain B1-mapping using three-dimensional DREAM. *Magn Reson Med*. 2019;82:924-934. doi:10.1002/mrm.27773
17. Tsao J. Ultrafast imaging: principles, pitfalls, solutions, and applications. *J Magn Reson Imaging*. 2010;32:252-266. doi:10.1002/jmri.22239
18. McRobbie DW, Moore EA, Graves MJ, Prince MR. *Acronyms Anonymous I: Spin Echo:185–206*. Cambridge University Press; 2017.
19. Layton KJ, Kroboth S, Jia F, et al. Pulseq: a rapid and hardware-independent pulse sequence prototyping framework. *Magn Reson Med*. 2017;77:1544-1552. doi:10.1002/mrm.26235
20. Ravi KS, Geethanath S, Vaughan JT. PyPulseq: a python package for MRI pulse sequence design. *J Open Source Softw*. 2019;4:1725.

21. Pruessmann KP, Weiger M, Börnert P, Boesiger P. Advances in sensitivity encoding with arbitrary K-space trajectories. *Magn Reson Med*. 2001;46:638-651.
22. Cerjanic A, Holtrop JL, Ngo GC, et al. PowerGrid: a open source library for accelerated iterative magnetic resonance image reconstruction. *Proceedings of the 24th Annual Meeting of ISMRM*. ISMRM; 2016:525.
23. Noll DC, Meyer CH, Pauly JM, Nishimura DG, Macovski A. A homogeneity correction method for magnetic resonance imaging with time-varying gradients. *IEEE Trans Med Imaging*. 1991;10:629-637. doi:10.1109/42.108599
24. Uecker M, Lai P, Murphy MJ, et al. ESPIRiT–an eigenvalue approach to autocalibrating parallel MRI: where SENSE meets GRAPPA. *Magn Reson Med*. 2014;71:990-1001. doi:10.1002/mrm.24751
25. Veldmann M, Ehses P, Chow K, Nielsen JF, Zaitsev M, Stöcker T. Open-source MR imaging and reconstruction workflow. *Magn Reson Med*. 2022;88:2395-2407. doi:10.1002/mrm.29384
26. Voelker MN, Kra O, Speck O, Ladd ME. Quality assurance phantoms and procedures for UHF MRI – the German ultrahigh field imaging (GUFI) approach. *Proceedings of the 26th Annual Meeting of ISMRM*. ISMRM; 2017:3912.
27. Breuer FA, Blaimer M, Heidemann RM, Mueller MF, Griswold MA, Jakob PM. Controlled aliasing in parallel imaging results in higher acceleration (CAIPIRINHA) for multi-slice imaging. *Magn Reson Med*. 2005;53:684-691.
28. Jenkinson M, Bannister P, Brady M, Smith S. Improved optimization for the robust and accurate linear registration and motion correction of brain images. *Neuroimage*. 2002;17:825-841.
29. Smith SM. Fast robust automated brain extraction. *Hum Brain Mapp*. 2002;17:143-155.
30. Koo TK, Li MY. A guideline of selecting and reporting Intraclass correlation coefficients for reliability research. *J Chiropr Med*. 2016;15:155-163.
31. Han Y, Du H, Lam F, Mei W, Fang L. Image reconstruction using analysis model prior. *Comput Math Methods Med*. 2016;2016:7571934. doi:10.1155/2016/7571934
32. Vannesjo SJ, Haeberlin M, Kasper L, et al. Gradient system characterization by impulse response measurements with a dynamic field camera. *Magn Reson Med*. 2013;69:583-593. doi:10.1002/mrm.24263

SUPPORTING INFORMATION

Additional supporting information may be found in the online version of the article at the publisher's website.

Table S1. Physical parameters and composition of the phantom used in phantom experiments.

Table S2. Measurement parameters of the spiral 3DREAM sequence for different resolutions. The abbreviations are as follows: tbp = time bandwidth product; int = accelerated spiral interleaves; Ph = phase encoding steps; R_{int} = in-plane acceleration; R_{Ph} = acceleration in phase-encoding direction; δ = CAIPIRINHA shift; ETL = echo train length; T_M = mixing time; T_S = STEAM preparation pulse interval; TA = acquisition time. "5 mm (RO)" refers to the spiral scan with modified signal separation gradients applied in readout direction.

Figure S1. (a) The sequence diagram of the modified Cartesian 3DREAM with an additional spoiler moment (highlighted in yellow) between the STE* and FID readouts to better separate the signals in k-space. (b) The sequence diagram of the spiral 3DREAM sequence (Figure 1) with signal separation gradients in slice direction.

Figure S2. Phantom experiments with different acceleration of the spiral 3DREAM sequence. Top row: One sagittal 5 mm slice in the phantom's center for a non-accelerated, accelerated, and non-accelerated segmented spiral scan. Bottom row: Scatterplots with linear fits for the comparison of the flip angle maps to the AFI sequence with normalized axes, corresponding to the three acceleration schemes. The selected region for the comparison is placed in the bottom-right hand corner. A white arrow points to a region with increased blurring at the bottom of the phantom, which is not present in the non-accelerated segmented scan.

Figure S3. Bland-Altman plot for the test-retest measurement of the spiral 3DREAM sequence. Solid lines represent the absolute mean difference of the two measurements and the limits of agreement, calculated as $1.96 \times \sigma$, where σ is the standard deviation.

Figure S4. One sagittal, coronal and transversal slice of the STE* at 5 mm resolution is shown for both Cartesian (top) and spiral (bottom) 3DREAM sequences. Additionally, the transversal slice of the FID is displayed on the right, with and without the FID filter applied.

Figure S5. To investigate the STE* decay, a fully sampled k-space of ones was synthesized with different spiral trajectories and the global filter was applied onto each interleaf. The FWHM of the reconstructed, zero-padded point spread function (PSF) shows the STE* blurring effect.

How to cite this article: Niesen S, Veldmann M, Ehses P, Stöcker T. Spiral 3DREAM sequence for fast whole-brain B1 mapping. *Magn Reson Med*. 2025;93:321-329. doi: 10.1002/mrm.30282